Passivity-Based Optimal State-Feedback Control for LCL-Filtered Grid-Following Converter

Gao, Chao; He, Shan; Song, Peiji; Davari, Pooya; Leung, Ka Nang; Chiang Loh, Poh; Blaabjerg, Frede

Published in:
I E E E Transactions on Power Electronics

DOI (link to publication from Publisher):
10.1109/TPEL.2024.3430383

Publication date:
2024

Document Version
Accepted author manuscript, peer reviewed version

Passivity-Based Optimal State-Feedback Control for LCL-Filtered Grid-Following Converter

Chao Gao, Shan He, *Member, IEEE*, Peiji Song, *Graduate Student Member, IEEE*, Pooya Davari, *Senior Member, IEEE*, Ka Nang Leung, *Senior Member, IEEE*, Poh Chiang Loh, and Frede Blaabjerg, *Fellow, IEEE*

***Abstract*—As the grid incorporates more voltage-source converters (VSCs), the stability issues arising from VSC-grid interactions escalate. While passivity theory offers a promising solution, existing passivity-based controller designs primarily rely on heuristic methods which do not advance stability beyond achieving passivity. To fully exploit the available degrees of freedom, this paper proposes employing an optimal state-feedback control that refines control parameters using an optimization algorithm. The optimization objective aims at maximizing the external stability by minimizing the product of 2-norms of the phase curve and magnitude curve of the VSC's output admittance. Compared with the conventional passivity-based design, the proposed control method improves the external stability with non-dissipative grid impedance and can mostly achieve dissipativity. The optimization algorithm and the process for generating starting points for the optimization are detailed. Experimental validations confirm the effectiveness of this optimal state-feedback control in enhancing VSC-grid interaction stability.**

***Index Terms*—Dissipation, state-feedback control, optimization, grid-following converter, LCL filter, impedance-based stability criterion.**

I. INTRODUCTION

As voltage-source converters (VSCs) are increasingly integrated into the power grid, ensuring their stability becomes paramount [1]. Controller designs that disregard the existence of grid impedance or solely account for inductive grid impedance prove inadequate in ensuring stability when faced with significant variations in grid impedances [2]. To simplify the analysis and assessment of stability under grid impedance, a stability criterion based on impedance was formulated [3], [4]. This criterion categorizes system stability into internal stability, focusing on the converter itself, and external stability, addressing the interaction between the VSC's output admittance and the power grid impedance. The introduction of passivity theory further strengthens this criterion by requiring passivity for both the VSC's output impedance and the grid impedance [5]. The advantage of this theory is that with all parts of the grid, i.e., grid-connected VSCs, grid impedance and other grid-connected loads, being passive, the equivalent grid impedance seen from any node remain passive, allowing the safe addition of new passive devices without risking instability [6]. However, as shown in [7], achieving passivity (dissipativity for all frequencies) is nearly impossible. Therefore, as a compromise, dissipativity is enforced below the Nyquist frequency in practice [7].

Considerable research efforts have been dedicated to achieving dissipativity of the converter's output admittance within the Nyquist frequency range. It has been observed that the non-dissipative frequency bands of a grid-connected converter fall into two main categories. The first category includes frequency bands around the resonant frequencies of the resonant (R) controller. This issue was first identified and resolved in [8] through a specific compensation angle of the R controller, along which a derivative-based calculation method was also proposed but exhibits complexity. Subsequently, a simplified alternative, the limit-based calculation method, was proposed as a substitute for the derivative-based approach [9].

The second category of non-dissipative region appears around the critical frequency, defined as a sixth of the sampling frequency when the total delay of computation and pulse-width modulation (PWM) is 1.5 times the sampling period. To address this issue, various methods have been proposed [10]–[14]. The classic approach involves using the capacitor current active damping (CCAD) with an optimal coefficient, as proposed in [11]. This achieves dissipativity below the Nyquist frequency and the real part of the output admittance become zero at the critical frequency, which also means the dissipativity at the critical frequency is vulnerable to the accuracy of the involved LCL parameters. To enhance robustness, several algorithms have been suggested. One category of algorithms involves inserting a first [12] or second [11] order lead-lag compensator in the CCAD path. Another option, proposed in [13], inserts a first-order lead or lag compensator in series with the current controller. Despite these efforts, the improvements are limited.

Apart from utilizing CCAD, there are also methods utilizing only the voltage of point of common coupling (PCC) to achieve dissipativity [15]–[17]. To maximize the utilization of available degrees of freedom and enhance overall passivity performance, some approach incorporates both voltage feedback and current feedback for passivity-based admittance shaping [18]–[20]. In [18], the optimal CCAD coefficient is first obtained with capacitor voltage feedback (CVF) omitted. However, after CVF is added, the designed CCAD coefficient becomes nonoptimal, non-dissipative region appearing around switching frequency. It then adopts multisampling technique to eliminate it. Multisampling technique expand dissipative frequency range by elevates the Nyquist frequency. However, it fails to realize dissipativity around the Nyquist frequency [18], [21]. Similar sequential parameter tuning processes are also adopted in [19], [20], where the non-dissipative region is tackled by adding low

(*Corresponding author*: *Shan He*.)

Chao Gao, Ka Nang Leung, and Poh Chiang Loh are with the Department of Electronic Engineering, the Chinese University of Hong Kong, Hong Kong, China (e-mail: chaogao@link.cuhk.edu.hk; knleung@ee.cuhk.edu.hk; pcloh@ee.cuhk.edu.hk).

Shan He, Pooya Davari, and Frede Blaabjerg are with the Department of Energy, Aalborg University, Aalborg 9220, Denmark (e-mail: shanhe@ieee.org; pda@energy.aau.dk; fbl@energy.aau.dk).

Peiji Song is with the Department of Information Engineering, the Chinese University of Hong Kong, Hong Kong, China (e-mail: sp020@ie.cuhk.edu.hk).

pass filter in CVF path. In summary, the conventional sequential tuning process consistently yields suboptimal parameters and poses challenges in achieving dissipativity.

All the previously mentioned methods rely on classical control theory, involving the modification of the system by introducing a specific transfer function at a certain point and adjusting the parameters within it. Usually, the transfer function is determined through practical experience, potentially leading to unnecessary complexity. Moreover, parameter tuning is often based on experience or observed trends. In cases with multiple parameters, they are usually tuned sequentially, preventing the attainment of an optimal result for a nonconvex problem [22]. Conversely, modern approaches seek to shift the tuning complexity into a computational tool, leveraging advanced optimization techniques [23]. This allows designers to concentrate on problem specification rather than intricate manual tuning. There is not much literature utilizing the modern approach for passivity-based design. In [24] and [25], a multi-objective robust H_∞ control is proposed with the restriction of output admittance being dissipative. In [26], the pole-placement method is employed without involving dissipativity requirement initially, subsequently achieving dissipativity by introducing a band-pass filter in the grid-side current feedforward path. However, these investigations conclude once dissipativity is attained, without making efforts to further improve it. Consequently, the dissipative property they confer is likely to be compromised with slight variations in physical parameters, or the system may be destabilized by even minor instances of non-dissipative grid impedance.

Addressing the previously outlined challenges, this paper presents a passivity-based optimal state-feedback control strategy. In contrast to conventional control systems, this method maximizes the stability in systems featuring non-dissipative grid impedance and can achieve dissipativity below the Nyquist frequency in most cases. This paper is structured as follows: Section II gives a brief review and analysis of conventional passivity-based designs, highlighting their non-optimal parameter configurations. Section III introduces the proposed optimal state-feedback control by defining the optimization problem, examining the feasible solution space, and employing the Complex method [27], [28] as the optimization algorithm. This section concludes with a comparative analysis of the robustness of the proposed method against traditional approaches. Experimental verifications are presented in Section IV followed by Section V, the Conclusion.

II. Analysis of Conventional Passivity-Based Controller Design

A. System Model

Fig. 1 shows the general schematic diagram of a three-phase grid-connected VSC. The grid-side current reference in dq frame ($i^*_{2,dq}$) is given by outer power loop which regulates the output active power or reactive power. Converter-side current (i_1) is sampled for control purposes and over-current protection. Grid-side current (i_2) is sampled for closed loop control. The capacitor voltage is sampled for capacitor voltage feedback (CVF) control and current synchronization through a phase-locked loop (PLL).

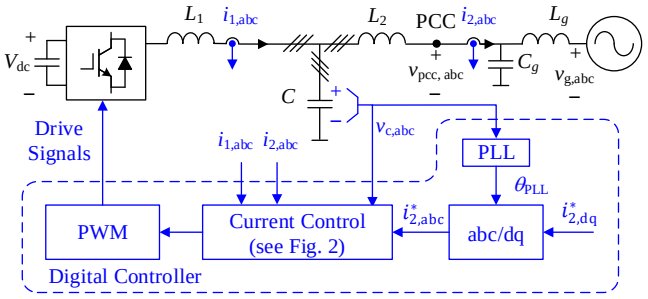

Fig. 1. Schematic diagram of a three-phase grid-connected VSC.

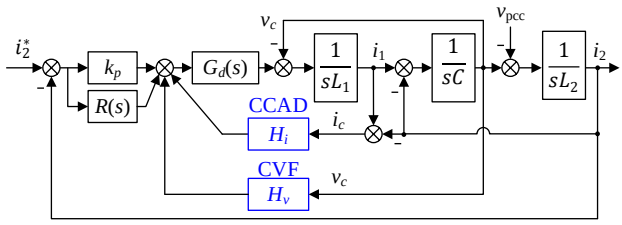

Fig. 2. Control block diagram of conventional passivity-based control in abc frame. (CCAD: capacitor current active damping, CVF: capacitor voltage feedback.)

Fig. 2 shows the control block diagram of conventional passivity-based control. All signals are in abc frame. CCAD and CVF are employed with coefficients of H_i and H_v respectively, where the capacitor current (i_c) is obtained by $i_1 - i_2$. i_2 is compared with i^*_2, and the error is regulated by a proportional resonant (PR) controller, which is expressed as:

$$PR(s) = k_p + \underbrace{\sum_h k_{rh} \frac{s\cos\varphi_h - h\omega_1 \sin\varphi_h}{s^2 + h^2\omega_1^2}}_{R(s)} \tag{1}$$

where ω_1 is the fundamental angle frequency, h is the order of the harmonics of concern, k_p is the proportional gain, k_{rh} and φ_h are the resonant gain and compensation angle of the R controller tuned at the resonant frequency, $h\omega_1$, respectively. All R controllers are collectively denoted by $R(s)$.

The one sampling period computational delay is modeled by e^{-sT_s} where T_s is the sampling period. The PWM and sampling process are collectively modeled by zero-order-hold (ZOH) divided by T_s [29]:

$$G_{ZOH}(s) = \frac{1 - e^{-sT_s}}{sT_s} \tag{2}$$

Thus, the total effect is the product of the two parts:

$$G_d(s) = e^{-sT_s} \frac{1 - e^{-sT_s}}{sT_s} \tag{3}$$

Therefore, i_2 can be expressed by

$$i_2 = G_{cl1}(s) i^*_2 - Y_{o1}(s) v_{pcc} \tag{4}$$

where v_{pcc} denotes the voltage at the PCC, $G_{cl1}(s)$ and $Y_{o1}(s)$ are closed loop transfer function and output admittance respectively. Their expressions are (5) and (6) given at the bottom of the next page.

B. Conventional Passivity-Based Controller Design

The impedance-based stability criterion states that the stability of a grid-connected converter is assured under two conditions: firstly, the closed-loop transfer function must be stable; secondly, the product of the grid impedance, $Z_g(s)$, and

the converter's output admittance, $Y_o(s)$, must meet the Nyquist stability criterion [3], [4]. A significant drawback of this criterion is that a complete reassessment of the stability is necessary with each alteration of the grid impedance. In response, the passivity theory has been introduced as an enhancement to the impedance-based stability criterion. This approach simplifies the second condition by requiring that both $Z_g(s)$ and $Y_o(s)$ exhibit dissipativity below the Nyquist frequency, characterized by a phase range of $[-90°, 90°]$. With both $Z_g(s)$ and $Y_o(s)$ dissipative, the Nyquist curve of their product, $Z_g(s)Y_o(s)$, will never encircle the point, -1, ensuring the stability. The passivity of $Z_g(s)$ is assured as long as it consists solely of passive components. Hence, the design of $Y_o(s)$ is decoupled from $Z_g(s)$, and the controller design target is to make $Y_o(s)$ dissipative below the Nyquist frequency while keeping the closed loop transfer function stable.

CCAD is a classic passivity-based control, and is usually conducted before other modifications are made. By setting H_v in $Y_{o1}(s)$ to zero, the effect of CVF on $Y_{o1}(s)$ is eliminated. Then H_i can be obtained by solving

$$Re\{Y_{o1}(s)\} \geq 0 \tag{7}$$

where $Re\{\cdot\}$ is the function returning the real part of the variable. The result is

$$H_i = \frac{36k_p}{L_1 C\omega_s^2} - k_p \tag{8}$$

where ω_s is the sampling angular frequency. The solving process of (8) can be found in [18], and will not be repeated here for brevity. k_p is related to the bandwidth of the closed-loop system, and is usually set to $0.1\omega_s L_1$ [11].

CVF is often preferred to improve transient performance and suppress the effect of v_{pcc} on output current. As suggested in [16], [21], the CVF coefficient smaller than one is preferable. Thus, H_v can be set to 0.9. Such kind of proportional CVF enhances the dissipativity around the critical frequency but spoils the dissipativity around the Nyquist frequency [18]. Since the combination of CCAD and CVF is identical to the control method described in [18] and serves as the basis for many advanced control methods developed in various papers [9], [11], [19], [20], [30], it is referred to as conventional control in this paper."

TABLE I
MAIN PARAMETERS OF THE SYSTEM AND VSC-I

Grid Parameters		
V_g	Grid phase voltage (RMS)	220 V
L_g	Grid inductance	4 mH
C_g	Grid capacitance	20 μF
VSC-I		
L_1	Converter-side inductance	4 mH
L_2	Grid-side inductance	2 mH
C	Filter capacitance	10 μF
S_n	Rated power	7 kVA
V_{dc}	DC-link voltage	700 V
f_{sw}	Switching frequency	5 kHz
f_s	Sampling frequency	5 kHz
k_{rh} for $h \in H$	Resonant current controller gain	2000 Ω/s

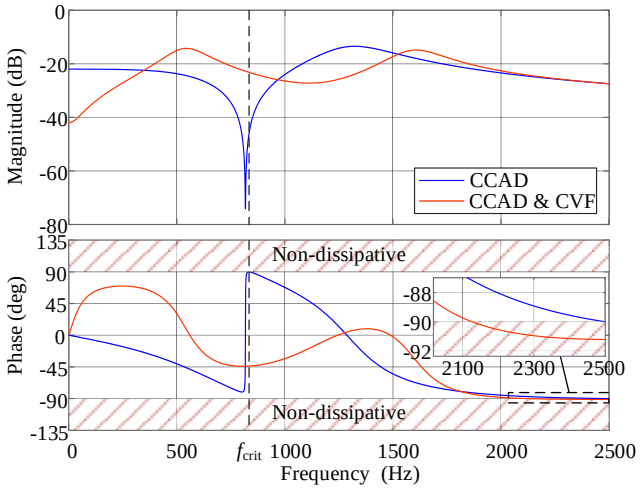

Fig. 3. Bode plots of VSC's output admittance with CCAD and combined CCAD and CVF.

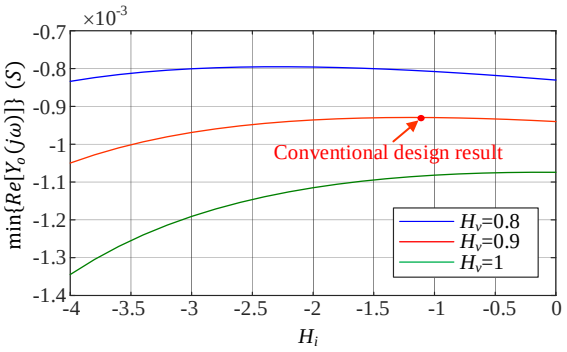

Fig. 4. Relationship between $\min\{Re[Y_{o1}(j\omega)]\}$, $\omega \in [0, \omega_s/2]$, and H_i and H_v.

With the parameters listed in Table I, the Bode plots of $Y_{o1}(s)$ using sole CCAD as well as both CCAD and CVF combined are illustrated in Fig. 3. As it can be seen, when using only CCAD, $Y_{o1}(s)$ (blue curve) is dissipative below the Nyquist frequency, and its phase curve is tangential to the 90° line at the critical frequency (f_{crit}) demonstrating zero dissipative margin. This situation is alleviated when CVF is added, as it can be seen from the red curve, the phase around f_{crit} is lifted demonstrating a certain amount of dissipative margin. However, the phase decreases below $-90°$ around the Nyquist frequency (2500 Hz) as presented by the zoom-in view indicating the shortage of dissipativity.

To summarize, the conventional passivity-based control cannot ensure the dissipativity below the Nyquist frequency with non-zero margin. This may partly be due to the parameter tuning process, the CCAD coefficient is given first without considering the existence of CVF, and the CVF coefficient is given by experience. Fig. 4 depicts the curves of $\min\{Re[Y_{o1}(j\omega)]\}$, $\omega \in [0, \omega_s/2]$, with respect to the CCAD coefficient, H_i, under three different H_v. A red point marks the conventional design outcome, which notably does not achieve the maximum $\min\{Re[Y_{o1}(j\omega)]\}$. It is observed that a smaller

$$G_{cl1}(s) = \frac{PR(s)G_d(s)}{s^3L_1L_2C - s^2L_2CH_iG_d(s) + s(L_1+L_2) - sL_2H_vG_d(s) + PR(s)G_d(s)} \tag{5}$$

$$Y_{o1}(s) = \frac{s^2L_1C - sCH_iG_d(s) - H_vG_d(s) + 1}{s^3L_1L_2C - s^2L_2CH_iG_d(s) + s(L_1+L_2) - sL_2H_vG_d(s) + PR(s)G_d(s)} \tag{6}$$

CVF coefficient (H_v=0.8) yields a larger $\min\{Re[Y_{o1}(j\omega)]\}$. It is noteworthy that a positive $\min\{Re[Y_{o1}(j\omega)]\}$ is expected which signifies the achievement of dissipativity below the Nyquist frequency. However, once dissipativity is assured, a larger $\min\{Re[Y_{o1}(j\omega)]\}$ does not necessarily signify a better performance. Generally, there remains degree of design freedom even after achieving dissipativity, and the subsequent design objective beyond dissipativity has not been thoroughly explored.

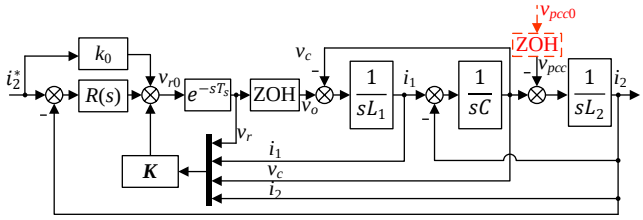

Fig. 5. Control block diagram of state feedback control.

III. Passivity-Based Optimal State-Feedback Control

A. Equivalence between Conventional Control and State-Feedback Control

Since the capacitor current (i_c) is obtained by $i_1 - i_2$, and fed back through H_i, it can thus be equivalently replaced by the feedback of i_1 and i_2 through H_i and $-H_i$ respectively. Considering that the PR controller also provides a proportional feedback path for i_2 by the proportional controller, the two i_2 proportional feedback paths can be combined yielding a feedback coefficient of $-k_p - H_i$.

The voltage reference (v_{r0}), upon being calculated, is retained within the controller until the end of the sampling period. This computational delay introduces one more state for the system, i.e., the output of the delay (v_r). Their relationship is:

$$v_r(k+1) = v_{r0}(k) \tag{9}$$

For conventional control, v_r is not utilized, and thus its feedback coefficient is zero. Consequently, the conventional control (see Fig. 2) is equivalent to the state feedback control depicted in Fig. 5 with the state feedback coefficient vector, $\boldsymbol{K}$, selected as follows:

$$\boldsymbol{K} = [k_1 \quad k_2 \quad k_3 \quad k_4] \tag{10}$$

$$\begin{cases} k_1 = -k_p - H_i \\ k_2 = H_i \\ k_3 = H_v \\ k_4 = 0 \end{cases} \tag{11}$$

where k_1, k_2, k_3, and k_4 are the feedback coefficients for i_2, i_1, v_c, and v_r respectively. Therefore, without involving additional sensors, full state feedback, which makes use of all four state variables, can be implemented. Moreover, better performance can be expected with optimization algorithm applied to the tuning of $\boldsymbol{K}$.

B. System Model with Full State Feedback Control

Fig. 5 shows the control block diagram of full state feedback control of LCL-filtered VSC. A R controller is added to eliminate steady-state error. However, the R controller can be omitted when designing the state feedback controller since it only affects the frequency characteristics around its resonant frequencies.

For full state feedback with $R(s)$ omitted, i_2 can be expressed by

$$i_2 = G_{cl2}(s) i_2^* - Y_{o2}(s) v_{pcc} \tag{12}$$

where $G_{cl2}(s)$ and $Y_{o2}(s)$ are closed-loop transfer function and output admittance respectively. Their expressions are (13) and (14) given at the bottom of this page, where $G_{d1}(s)$ is expressed as

$$G_{d1}(s) = \frac{e^{-sT_s}}{1 - e^{-sT_s}k_4} \times \frac{1 - e^{-sT_s}}{sT_s} \tag{15}$$

C. Optimization Problem Formulation

$\boldsymbol{K}$ is responsible to equip the VSC with expected properties. Specifically, the objectives are twofold: firstly, the closed-loop transfer function must be stable; secondly, the VSC's output admittance should not only be dissipative but also strive to maximize the external stability considering the presence of the non-dissipative grid impedance wherever feasible. These design goals need to be encapsulated within an optimization problem, with $\boldsymbol{K}$ serving as the adjustable parameter.

However, the challenge arises from the limitations of passivity theory, which primarily addresses the concept of dissipativity as a binary condition, without commenting on how to further improve external stability based on dissipativity. Despite the scarcity of discussion on this topic in existing literature, an insight can be derived from the foundational principles of the passivity theory, specifically the impedance-based stability criterion. This criterion includes a vital condition: the product of the grid impedance, $Z_g(s)$, and the output admittance, $Y_{o2}(s)$, must meet the Nyquist stability criterion. Given that $Z_g(s)$ is variable and typically unknown, aligning the phase angle of $Y_{o2}(s)$ closer to zero ensures that $\angle Z_g(s)Y_{o2}(s)$ remains well away from 180°, effectively maximizing the phase margin (PM) of $Z_g(s)Y_{o2}(s)$. Additionally, reducing the magnitude of $Y_{o2}(s)$ decreases the overall magnitude of $Z_g(s)Y_{o2}(s)$, thereby enhancing stability by preventing the Nyquist curve of $Z_g(s)Y_{o2}(s)$ from passing through the unit circle. Another interpretation is that minimizing the magnitude of $Z_g(s)Y_{o2}(s)$ maximizes its gain margin. In summary, it is favorable for $Y_{o2}(s)$ to exhibit a phase curve that approaches zero and to have a reduced magnitude curve, which structures the following optimization problem:

$$\begin{cases} \underset{\boldsymbol{K}}{\text{minimize}} \ \|\angle Y_{o2}(j\omega)\|_2 \times \|Y_{o2}(j\omega)\|_2 \\ \text{subject to} \ \ G_{cl2}(s) \text{ is stable.} \end{cases} \tag{16}$$

where $\|\cdot\|_2$ denotes the 2-norm operation [31], which is defined by

$$G_{cl2}(s) = \frac{k_0 G_{d1}(s)}{s^3 L_1 L_2 C - s^2 L_2 C k_2 G_{d1}(s) + s(L_1 + L_2) - sL_2 k_3 G_{d1}(s) - (k_1 + k_2) G_{d1}(s)} \tag{13}$$

$$Y_{o2}(s) = \frac{s^2 L_1 C - sC k_2 G_{d1}(s) - k_3 G_{d1}(s) + 1}{s^3 L_1 L_2 C - s^2 L_2 C k_2 G_{d1}(s) + s(L_1 + L_2) - sL_2 k_3 G_{d1}(s) - (k_1 + k_2) G_{d1}(s)} \tag{14}$$

$$\|a(\omega)\|_2 = \sqrt{\int_0^{\frac{\omega_s}{2}} |a(\omega)|^2 d\omega} \tag{17}$$

where the upper bound of the integral is set to half of the sampling frequency because that is the frequency band of interest.

The first term, $\|\angle Y_{o2}(j\omega)\|_2$, in (16) pushes $\angle Y_{o2}(j\omega)$ to zero to meet the phase requirement, thereby encouraging $Y_{o2}(s)$ to be dissipative. The second term, $\|Y_{o2}(j\omega)\|_2$, restricts the magnitude of $Y_{o2}(j\omega)$ to meet the magnitude requirement. The 2-norm operation is utilized because of the square in it penalizes the larger value harder. The two optimization objectives are combined through multiplication because achieving either objective effectively reduces the importance of achieving the other. For example, if $\|\angle Y_{o2}(j\omega)\|_2$ is optimized to zero, then the magnitude of $Y_{o2}(j\omega)$ becomes irrelevant. On the contrary, in cases when dissipativity cannot be achieved, the optimization will strive to reduce the magnitude of $Y_{o2}(j\omega)$ which also maximizes its external stability. Therefore, the proposed method does not necessarily result in an output admittance that is dissipative below the Nyquist frequency. Instead, its primary objective is to maximize external stability. The feasible region ensures the optimization result to stabilize $G_{cl2}(s)$.

However, within the *s*-domain, assessing the stability of $G_{cl2}(s)$ through the Nyquist criterion relies on graphical analysis, which poses challenges for a computer-based algorithm. Moreover, the presence of exponential functions, such as e^{-sT_s}, further complicates the calculation of the poles of $G_{cl2}(s)$, rendering it to be impractical. Consequently, the subsequent section will reinterpret the feasible region within the *z*-domain, offering a more practical approach for analysis.

D. Analysis of Feasible Region

In discrete state-space model, the nonlinear terms, e^{-sT_s} and $G_{ZOH}(s)$, can naturally be integrated into the model. First of all, the state space model of the LCL-filtered VSC in continuous domain is

$$\begin{cases} \dfrac{d\boldsymbol{x}(t)}{dt} = \boldsymbol{A}\boldsymbol{x}(t) + \boldsymbol{B_1} v_o(t) + \boldsymbol{B_2} v_{pcc}(t) \\ y(t) = \boldsymbol{C}\boldsymbol{x}(t) \end{cases} \tag{18}$$

$$\boldsymbol{x}(t) = \begin{bmatrix} i_2(t) \\ i_1(t) \\ v_c(t) \end{bmatrix}, \boldsymbol{A} = \begin{bmatrix} 0 & 0 & 1/L_2 \\ 0 & 0 & -1/L_1 \\ -1/C & 1/C & 0 \end{bmatrix}$$
$$\boldsymbol{B_1} = \begin{bmatrix} 0 \\ 1/L_1 \\ 0 \end{bmatrix}, \boldsymbol{B_2} = \begin{bmatrix} -1/L_2 \\ 0 \\ 0 \end{bmatrix}, \boldsymbol{C} = [1 \quad 0 \quad 0] \tag{19}$$

Through ZOH discretization [32], the continuous-time model (18) can be discretized as

$$\begin{cases} \boldsymbol{x}(k+1) = \boldsymbol{\Phi}\boldsymbol{x}(k) + \boldsymbol{P} v_r(k) + \boldsymbol{Q} v_{pcc0}(k) \\ y(k) = \boldsymbol{C}\boldsymbol{x}(k) \end{cases}$$
$$\boldsymbol{\Phi} = e^{\boldsymbol{A}T_s} \tag{20}$$
$$\boldsymbol{P} = \boldsymbol{A}^{-1}(e^{\boldsymbol{A}T_s} - \boldsymbol{I})\boldsymbol{B_1}$$
$$\boldsymbol{Q} = \boldsymbol{A}^{-1}(e^{\boldsymbol{A}T_s} - \boldsymbol{I})\boldsymbol{B_2}$$

which incorporates the ZOH immediately after all input variables. Thus, the input variables are shifted from v_o and v_{pcc} to v_r and v_{pcc0} respectively, which feed the ZOHs before v_o and v_{pcc} respectively (see Fig. 5). Note that the ZOH before v_{pcc} (red dashed line) does not exist in reality, this is one of the discrepancies between the discrete-time state space model and the reality. Therefore, the output admittance derived from the discrete model (20) will be the transfer function i_2/v_{pcc0}, which includes an extra ZOH compared with the expected i_2/v_{pcc}, as represented by (6) and (14). Consequently, to ensure an accurate assessment of external stability, the output admittance from the s-domain model as specified in equations (6) and (14) will continue to be utilized.

Considering (9), the computational delay can be readily incorporated into the discrete-time state space model:

$$\begin{cases} \boldsymbol{x}_1(k+1) = \underbrace{\begin{bmatrix} \boldsymbol{\Phi} & \boldsymbol{P} \\ \boldsymbol{0}_{3\times1} & 0 \end{bmatrix}}_{\boldsymbol{\Phi_1}} \boldsymbol{x}_1(k) + \underbrace{\begin{bmatrix} \boldsymbol{0}_{3\times1} \\ 1 \end{bmatrix}}_{\boldsymbol{P_1}} v_{r0}(k) + \underbrace{\begin{bmatrix} \boldsymbol{Q} \\ 0 \end{bmatrix}}_{\boldsymbol{Q_1}} v_{pcc0}(k) \\ y(k) = \underbrace{[1 \quad 0 \quad 0 \quad 0]}_{\boldsymbol{C_1}} \boldsymbol{x}_1(k) \end{cases} \tag{21}$$

where $\boldsymbol{x_1}(k) = [\boldsymbol{x}(k) \quad v_r(k)]^T$. Through state transformation:

$$\boldsymbol{x_c}(k) = \boldsymbol{T}\boldsymbol{x_1}(k) \tag{22}$$

the system (21) can be converted into a controllable canonical form [33], of which the state equation is given as

$$\boldsymbol{x_c}(k+1) = \underbrace{\begin{bmatrix} 0 & 1 & 0 & 0 \\ 0 & 0 & 1 & 0 \\ 0 & 0 & 0 & 1 \\ a_1 & a_2 & a_3 & a_4 \end{bmatrix}}_{\boldsymbol{\Phi_c}} \boldsymbol{x_c}(k) + \underbrace{\begin{bmatrix} \boldsymbol{0}_{3\times1} \\ 1 \end{bmatrix}}_{\boldsymbol{P_c}} v_{r0}(k) + \boldsymbol{T}\boldsymbol{Q_1} v_{pcc0}(k) \tag{23}$$

where $\boldsymbol{\Phi_c} = \boldsymbol{T}\boldsymbol{\Phi_1}\boldsymbol{T}^{-1}$, and $\boldsymbol{P_c} = \boldsymbol{T}\boldsymbol{P_1}$. $\boldsymbol{T}$ should be chosen as follows:

$$\boldsymbol{T} = \begin{bmatrix} \boldsymbol{t_1} \\ \boldsymbol{t_1}\boldsymbol{\Phi_1} \\ \boldsymbol{t_1}\boldsymbol{\Phi_1^2} \\ \boldsymbol{t_1}\boldsymbol{\Phi_1^3} \end{bmatrix} \tag{24}$$

where the row vector $\boldsymbol{t_1}$ is computed as:

$$\boldsymbol{t_1} = [0 \quad 0 \quad 0 \quad 1]/[\boldsymbol{P_1} \quad \boldsymbol{\Phi_1}\boldsymbol{P_1} \quad \boldsymbol{\Phi_1^2}\boldsymbol{P_1} \quad \boldsymbol{\Phi_1^3}\boldsymbol{P_1}] \tag{25}$$

The control law of full state feedback is:

$$v_{r0}(k) = \boldsymbol{K}\boldsymbol{x_1}(k) + k_p i_2^*(k) \tag{26}$$

With the transformation of (22), (26) can be equivalently transformed into

$$v_{r0}(k) = \boldsymbol{K_c}\boldsymbol{x_c}(k) + k_p i_2^*(k) \tag{27}$$

where

$$\boldsymbol{K_c} = \boldsymbol{K}\boldsymbol{T}^{-1} = [k_{c1} \quad k_{c2} \quad k_{c3} \quad k_{c4}] \tag{28}$$

Substituting (27) into (23) gives the closed loop state equation:

$$\boldsymbol{x_c}(k+1) = \underbrace{\begin{bmatrix} 0 & 1 & 0 & 0 \\ 0 & 0 & 1 & 0 \\ 0 & 0 & 0 & 1 \\ a_1 + k_{c1} & a_2 + k_{c2} & a_3 + k_{c3} & a_4 + k_{c4} \end{bmatrix}}_{\boldsymbol{\Phi_2}} \boldsymbol{x_c}(k) + \boldsymbol{P_c} k_p i_2^*(k) + \boldsymbol{T}\boldsymbol{Q_1} v_{pcc0}(k) \tag{29}$$

where $\boldsymbol{\Phi_2} = \boldsymbol{\Phi_c} + \boldsymbol{P_c}\boldsymbol{K_c}$. The stability of the closed loop discrete system, (29), is equivalent to the stability of the original

continuous system (12). Therefore, the feasible region of the optimization problem (16) can be replaced by

$$|\lambda(\boldsymbol{\Phi_2})| \le r \tag{30}$$

where r is an adjustable value and should be smaller than one. $\lambda(\boldsymbol{\Phi_2})$ returns all eigenvalues of $\boldsymbol{\Phi_2}$, i.e., the roots of the characteristic equation, i.e.,

$$\begin{aligned}|\lambda \boldsymbol{I_{4\times4}} - \boldsymbol{\Phi_2}| &= \lambda^4 - (a_4 + k_{c4})\lambda^3 - (a_3 + k_{c3})\lambda^2 \\ &\quad -(a_2 + k_{c2})\lambda - (a_1 + k_{c1}) \\ &= (\lambda^2 + b_1\lambda + c_1)(\lambda^2 + b_2\lambda + c_2) = 0\end{aligned} \tag{31}$$

where $\boldsymbol{I_{4\times4}}$ is a unit matrix of 4th order, and b_1, c_1, b_2, and c_2 have the following relationships with k_{c1}, k_{c2}, k_{c3}, and k_{c4}.

$$\begin{cases} k_{c1} = -c_1 c_2 - a_1 \\ k_{c2} = -b_1 c_2 - b_2 c_1 - a_2 \\ k_{c3} = -c_1 - c_2 - b_1 b_2 - a_3 \\ k_{c4} = -b_1 - b_2 - a_4 \end{cases} \tag{32}$$

Therefore, (30) is equivalent to the following equations

$$\left|\frac{-b_1 \pm \sqrt{b_1^2 - 4c_1}}{2}\right| \le r \tag{33}$$

$$\left|\frac{-b_2 \pm \sqrt{b_2^2 - 4c_2}}{2}\right| \le r \tag{34}$$

When r assumes its maximum, 1, solving (33) and (34) yields

$$\begin{bmatrix} -1 & -1 \\ 1 & -1 \\ 0 & 1 \end{bmatrix} \begin{bmatrix} b_1 \\ c_1 \end{bmatrix} \le \begin{bmatrix} 1 \\ 1 \\ 1 \end{bmatrix} \tag{35}$$

$$\begin{bmatrix} -1 & -1 \\ 1 & -1 \\ 0 & 1 \end{bmatrix} \begin{bmatrix} b_2 \\ c_2 \end{bmatrix} \le \begin{bmatrix} 1 \\ 1 \\ 1 \end{bmatrix} \tag{36}$$

The solution of (33) is detailed in Appendix, which is also applicable to (34) with b_1 and c_1 replaced by b_2 and c_2. The feasible region represented by (35) and (36) is visualized in Fig. 6 as the shaded triangle, i.e., I ⋂ II. Obviously, when $r < 1$, the feasible region is inside the shaded area.

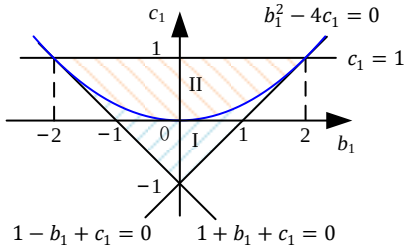

Fig. 6. Illustration of feasible region.

It is natural to use $\boldsymbol{J} = [b_1 \quad c_1 \quad b_2 \quad c_2]$ as decision variables instead of the original $\boldsymbol{K}$ since the boundary and feasible region of $\boldsymbol{J}$ is clearer and well defined. In this way, the optimization problem, (16), can be rewritten as:

$$\begin{cases} \underset{\boldsymbol{J}}{\text{minimize}}\ F(\boldsymbol{J}) = \|\angle Y_{o2}(j\omega)\|_2 \times \|Y_{o2}(j\omega)\|_2 \\ \text{subject to } |\lambda(\boldsymbol{\Phi_2})| \le r \end{cases} \tag{37}$$

where the feasible region can be expanded to (33) and (34). $F(\boldsymbol{J})$ is the objective function, and $Y_{o2}(s)$ is now calculated from $\boldsymbol{J}$ through (32), (28) and (14). The analytical expression of $Y_{o2}(s)$ in terms of $\boldsymbol{J}$ is complex and unnecessary for computer-based algorithm. As it will be seen in the next subsection, only the evaluation of $Y_{o2}(s)$ is enough for the optimization algorithm.

E. Optimization Algorithm

The optimization problem in (37) is obviously nonlinear. Considering it is difficult to calculate the derivative of the objective function, $dF(\boldsymbol{J})/d\boldsymbol{J}$, the optimization algorithm should not involve derivatives. There are various optimization algorithms that can be employed, among which this paper adopts the Complex method [27], [28] to illustrate the solving process. The Complex method needs only the objective function value to search for the global minimizer featuring easy implementation [27], [28].

At the beginning of the algorithm, n starting points are generated randomly. n is usually set bigger than the dimension of the decision variable, which is 4 in the study case. Thus, n is set to 10 in this paper. Given the feasible region defined by (33) and (34), the starting points can be generated through the following procedures:

1) Assign two random values, each between -2 and 2, to b_1 and b_2, respectively.

2) Assign two random values, each between -1 and 1, to c_1 and c_2, respectively.

3) Verify the feasibility of the generated $\boldsymbol{J}$ using conditions (33) and (34). If $\boldsymbol{J}$ is deemed infeasible, discard it. Repeat these three steps until a sufficient number of starting points have been generated.

Then the objective function is evaluated at all points. The worst point, $\boldsymbol{J_{worst}}$, featuring the largest objective function value is replaced by a new point, $\boldsymbol{J_{new}}$, obtained by reflecting $\boldsymbol{J_{worst}}$ through the centroid of the remaining points, $\boldsymbol{J_c}$, in the complex. The centroid, $\boldsymbol{J_c}$, of the points in the complex excluding $\boldsymbol{J_{worst}}$, could be calculated according to:

$$\boldsymbol{J_c} = \frac{1}{k-1}\left[\left(\sum_{i=1}^{k} \boldsymbol{J_i}\right) - \boldsymbol{J_{worst}}\right] \tag{38}$$

$\boldsymbol{J_{new}}$ is now calculated as the reflection of $\boldsymbol{J_{worst}}$ through $\boldsymbol{J_c}$ by a factor α, i.e.,

$$\boldsymbol{J_{new}} = \boldsymbol{J_c} + \alpha(\boldsymbol{J_c} - \boldsymbol{J_{worst}}) \tag{39}$$

The reflection coefficient α is set to 1.3 according to [28]. If $\boldsymbol{J_{new}}$ is feasible and $F(\boldsymbol{J_{new}})$ is smaller than $F(\boldsymbol{J_{worst}})$, $\boldsymbol{J_{worst}}$ is replaced by $\boldsymbol{J_{new}}$ and the procedure starts over by reflecting the new worst point in the new complex. If $\boldsymbol{J_{new}}$ is infeasible or still the worst it is moved halfway towards $\boldsymbol{J_c}$, i.e.,

$$\boldsymbol{J_{new}} = \boldsymbol{J_c} + \frac{\alpha}{2}(\boldsymbol{J_c} - \boldsymbol{J_{worst}}) \tag{40}$$

Such a procedure of moving the worst $\boldsymbol{J_{new}}$ towards $\boldsymbol{J_c}$ is repeated until $\boldsymbol{J_{new}}$ is feasible and better than $\boldsymbol{J_{worst}}$. The reflecting procedure is continuously carried out until the following condition is satisfied:

$$\|\boldsymbol{J_{best}} - \boldsymbol{J_{worst}}\|_\infty < \varepsilon \tag{41}$$

where ε is a prescribed small value and is set to 0.0001 in this paper, and $\boldsymbol{J_{best}}$ is the best point in current complex featuring the smallest objective function value. The infinity-norm, $\|\cdot\|_\infty$, returns the maximum absolute value of all its entries. Then, $\boldsymbol{J_{best}}$ is the best decision variable yielded by the optimization algorithm.

F. Tuning of Other Parameters

Generally, it is expected that the output has no steady state error when the R controller is omitted. Thus, k_0 should satisfy the following equation

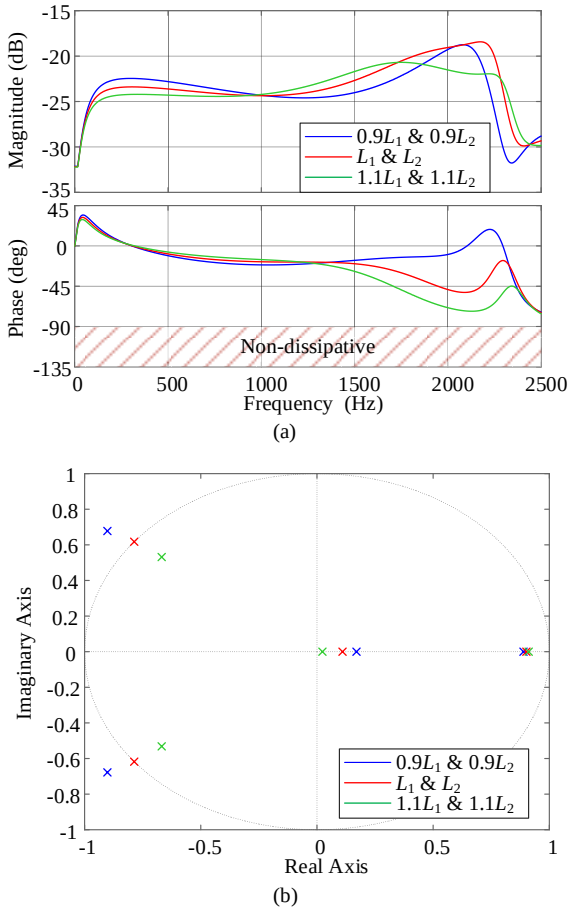

Fig. 7. Sensitivity analysis of optimization results. (a) Bode plots of $Y_{o2}(s)$, and (b) its corresponding closed-loop pole maps using the optimization result with $r = 1$, along with real parameters, L_1 and L_2, drifting.

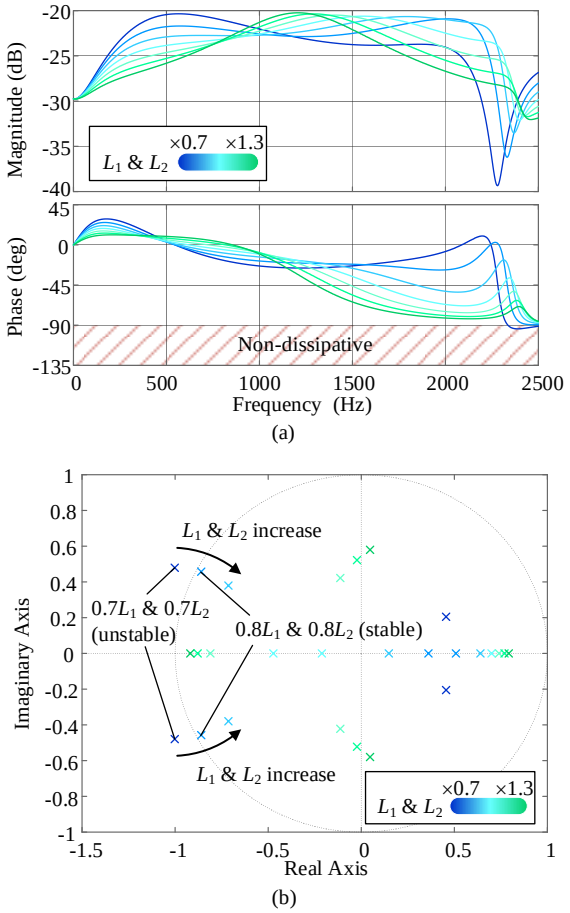

Fig. 8. Sensitivity analysis of optimization results. (a) Bode plots of $Y_{o2}(s)$, and (b) its corresponding closed-loop pole maps using the optimization result with $r = 0.7$, along with real parameters, L_1 and L_2, drifting.

$$|G_{cl2}(j\omega_1)| = 1 \tag{42}$$

That is, the closed loop gain at fundamental frequency is one [34]. Solving (42) yields k_0.

The R controller is also indispensable to ensure no steady state error especially when the physical parameters drift. As indicated by [9], R controller can introduce non-dissipative region around its resonant frequency unless the compensation angle is set to:

$$\varphi_h = -\angle\left[\frac{G_{d1}(s)}{s^2L_1C - sCk_2G_{d1}(s) - k_3G_{d1}(s) + 1}\right]_{s=jh\omega_1} \tag{43}$$

The derivation of (43) can be found in [9] and will not be included in this paper for brevity.

G. Robustness Analysis of the Optimization Result

For grid-connected converter, the filter capacitor usually adopts film capacitor whose capacitance is generally limited to ±5% of its nominal value throughout its service life [35], whereas the inductance can drop by 20% of its nominal value because of the core saturation [36]. Therefore, only the robustness analysis under drifting inductance will be conducted in this subsection.

With r set to 1, and relevant parameters listed in Table I, the optimization result, $\boldsymbol{J}$, is obtained by the Complex method and listed in Table II, alongside the corresponding state feedback vector, $\boldsymbol{K}$. Fig. 7 presents the Bode plots of $Y_{o2}(s)$, and the closed-loop pole map using the resultant $\boldsymbol{K}$, along with the real parameters, L_1 and L_2 drifting from 0.9 to 1.1 times its nominal value. The pole map is obtained by solving the characteristic equation (31). Dissipativity is achieved below the Nyquist frequency with enough distance to $\pm 90°$ boundaries (see Fig. 7(a)). However, since $r = 1$, poles are pushed to unit circle indicating no stability margin. As it can be seen from Fig. 7(b), the poles will move out of the unit circle as the inductances decrease. Therefore, to reserve enough stability margin for the system, r is set to 0.7 to limit the poles within the circle with a radius of 0.7. The corresponding optimization results are listed in Table II.

The Bode plot of $Y_{o2}(s)$, and the closed-loop pole map of the proposed state feedback control with $r = 0.7$ is shown in Fig. 8. First of all, the phase curves of $Y_{o2}(s)$ remain within the range of $[-90°, 90°]$ below the Nyquist frequency, with the exception of the scenario where L_1 and L_2 are reduced to 0.7 times their original values, at which point it becomes non-dissipative around the Nyquist frequency.

Compared to the Bode plot of the output admittance with the conventional control (red line in Fig. 3), the phase curve with proposed control (see Fig. 8(a)) is flat and closer to zero, and

TABLE II
OPTIMIZATION RESULTS OF PROPOSED STATE FEEDBACK CONTROL

r	$\boldsymbol{J}$	$\boldsymbol{K}$
1	$[-1.04 \quad 0.04 \quad 1.58 \quad 1.0]$	$[14.01 \quad -14.26 \quad 2.22 \quad -1.23]$
0.7	$[0.68 \quad 0.10 \quad -0.23 \quad -0.33]$	$[-1.14 \quad -9.04 \quad 1.81 \quad -1.13]$

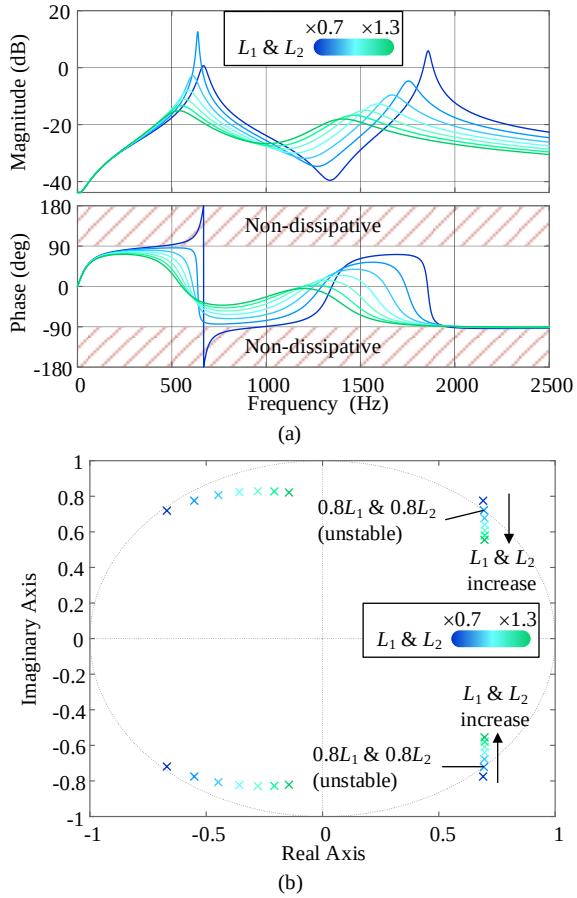

Fig. 9. Sensitivity analysis of conventional method. (a) Bode plots of $Y_{o1}(s)$, and (b) its corresponding closed-loop pole maps using the conventional control, along with real parameters, L_1 and L_2, drifting.

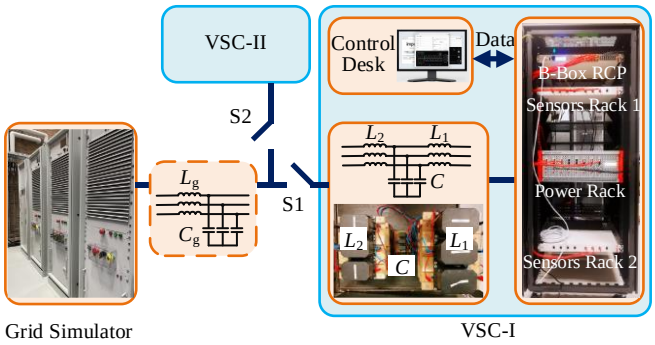

Fig. 10. Experimental setup using two three-phase LCL-filtered VSCs and a grid simulator.

the magnitude curve is also flat and smaller indicating an improvement in external stability. Besides, a smaller magnitude in the output admittance is favorable since the influence of v_{pcc} on i_2 is smaller. Furthermore, by setting r to 0.7, the poles retreat back into the unit circle, enabling the system to maintain stability even with L_1 and L_2 reducing to 0.8 times their nominal values (see Fig. 8(b)).

Additionally, the Bode plots of $Y_{o1}(s)$ and the pole map of the conventional control are presented in Fig. 9. The phase curve of $Y_{o1}(s)$ starts to become non-dissipative around the critical frequency ($\frac{\omega_s}{6} \approx 833$ Hz) when L_1 and L_2 decrease to 0.7 times their nominal values. Besides, all phase curves pass through $-90°$ line around 2000 Hz, that is, $Y_{o1}(s)$ is non-dissipative around the Nyquist frequency. The closed-loop pole map (Fig. 9 (b)) indicates that the with -20% parameter drift, the system will become unstable, which is less robust than the proposed optimal state feedback control (see Fig. 8(b)). Note that the pole map of conventional control is obtained by equivalently converting it to state feedback control using (11), and then solving the characteristic equation (31).

IV. Experimental Verification

To demonstrate the theoretical analysis, experiments were conducted on two three-phase grid-connected VSCs equipped with an LCL filter, as depicted in Fig. 10. VSC-I and VSC-II are identical in hardware expect for their LCL filter. The grid emulation was accomplished using a high-fidelity linear amplifier APS 15000. The half-bridge module of VSC-I and VSC-II and their corresponding control platform are sourced from an Imperix system, consisting of a PEB-SiC-8024 module and a B-BOX RCP control platform, respectively.

A. Internal Stability Validation

According to the impedance-based stability criterion, the internal stability is the prerequisite for the system's stability. To verify the internal stability of both conventional control and proposed state feedback control, both control schemes are implemented in VSC-I separately with no grid impedance, that is, the dashed part in Fig. 10 is removed. S1 in Fig. 10 is closed and S2 in Fig. 10 is open. Only resonant controller tuned at the fundamental frequency is implemented for both controls. Fig. 11(a) and (b) present the experimental results using conventional control and proposed state feedback control respectively. The PWM of the VSC is enabled at 0.04 s. During the subsequent 0.04 s, the q-axis current reference is set to 0, and d-axis current reference is given by the DC-link voltage regulator to establish a 700 V DC-link voltage. Note that the DC-link of VSC is a sole capacitor without DC source. Then, in the following 0.04 s, DC-link voltage has been established and the d-axis current reference reduces to about zero. Meanwhile, the q-axis current reference is set to 15 A in magnitude. As it can be seen from Fig. 11(a) and (b), both controllers operate stably. This is in consistency with the pole maps shown in Fig. 8(b) and Fig. 9(b).

B. Stability Validation with Passive Grid Impedance

Except for the non-dissipative region around the Nyquist frequency of the conventional control, both the conventional control and the proposed control are dissipative below the Nyquist frequency. Thus, they are stable when connected to a grid with a passive grid impedance. To verify their stability with passive grid impedance, L_g and C_g are connected into the circuit as shown in the dashed part in Fig. 10. Their parameters are shown in Table I. Therefore, the grid admittance will be:

$$Y_g(s) = sC_g + \frac{1}{sL_g} \tag{44}$$

Fig. 12 presents the frequency responses of $Y_g(s)$ (black line) along with those of VSC-I's output admittances using conventional control (blue line) and proposed control (red line). Only the resonant controller tuned at fundamental frequency is implemented for both control methods. As it can be seen, all PMs are positive indicating that both control methods can

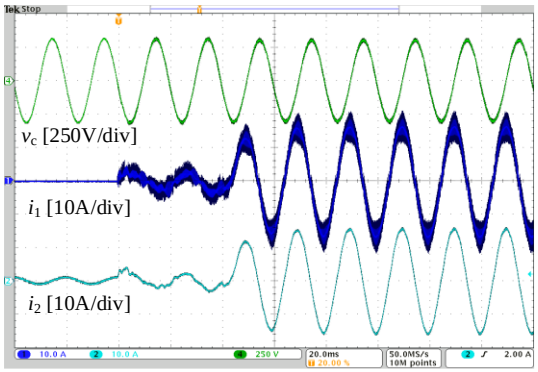

(a)

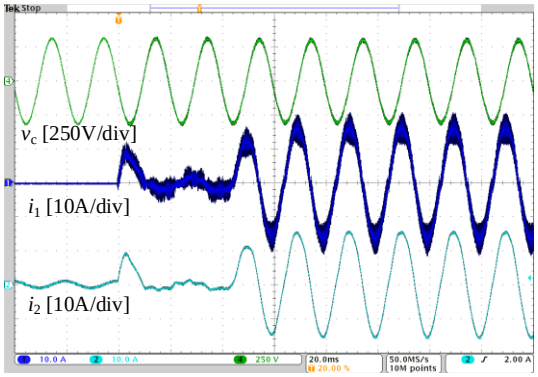

(b)

Fig. 11. Experimental results for stability verification with no grid impedance using (a) conventional control, and (b) proposed state feedback control.

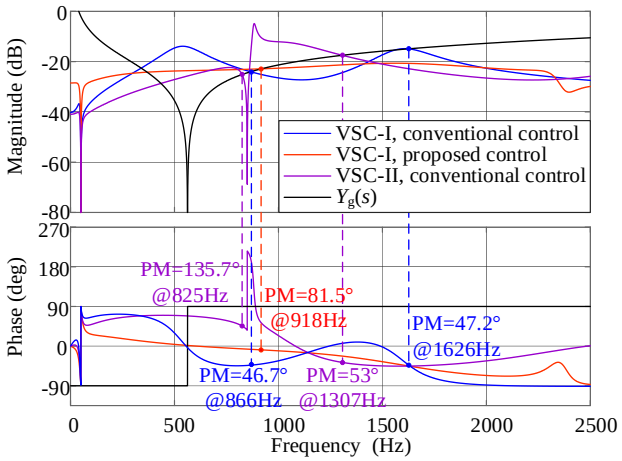

Fig. 12. Frequency responses of the grid admittance, $Y_g(s)$, and the VSC's output admittances using conventional control and the proposed control.

stabilize the system.

The corresponding experimental results are shown in Fig. 13(a) and (b). The starting process is the same as that in Section IV-A and will not be repeated here. Obviously, both control methods result in a stable waveform in consistency with the analysis of Fig. 12.

C. Stability Validation with Non-Dissipative Grid Impedance

The large phase absolute value of the output admittance using conventional control tends to destabilize the system with non-dissipative grid impedance. To verify this, VSC-II is connected to the grid, and its parameters are listed in Table III. VSC-II adopts the same conventional control as detailed in Section II-B. Two R controllers are implemented in VSC-II. One is tuned

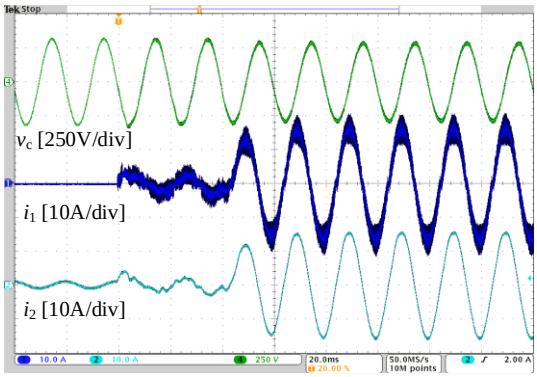

(a)

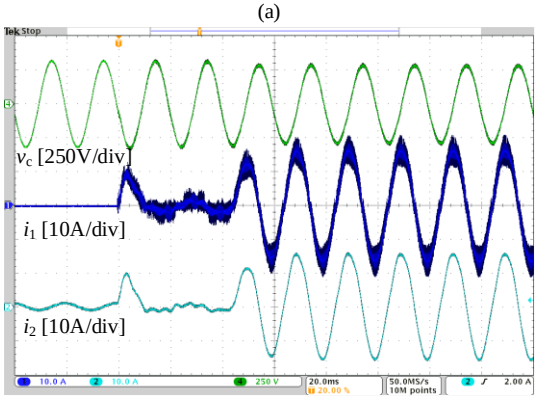

(b)

Fig. 13. Experimental results for stability verification with $L_g = 4\ mH$, and $C_g = 20\ \mu F$ using (a) conventional control, and (b) proposed state feedback control.

TABLE III
MAIN PARAMETERS OF VSC-II

L_1	Converter-side inductance	2 mH
L_2	Grid-side inductance	1 mH
C	Filter capacitance	5 μF
S_n	Rated power	7 kVA
V_{dc}	DC-link voltage	700 V
f_{sw}	Switching frequency	10 kHz
f_s	Sampling frequency	10 kHz
k_{rh} for $h \in H$	Resonant current controller gain	2000 Ω/s

at fundamental frequency with the compensation angle set the same as (43). The other is tuned at the 17th order harmonic with the compensation angle set to zero. It is worth noting that generally a series of R controllers tuned at the 1st, 5th, 7th, 11th, 13th, 17th, and 19th order harmonics should be added to the controller for suppressing harmonic current arising from harmonic voltage. However, in this paper, for clearly demonstrating the effect of a single harmonic R controller, only the 17th harmonic R controller is added for harmonic control.

The output admittance of VSC-II, $Y_{o1,VSC-II}(s)$, is also shown in Fig. 12. Obviously, it is dissipative around the fundamental frequency because of the correct compensation angle used. However, around 17th order harmonic frequency, its phase curve exceeds 90° largely resulting in non-dissipative region because of the incorrect compensation angle. Notwithstanding, VSC-II can stabilize the system since all PMs are positive.

When both VSC-I and VSC-II are connected to the grid, the admittance of VSC-II is a part of grid admittance in the point of view of VSC-I. The equivalent grid admittance, $Y_{g,eq}(s)$, is:

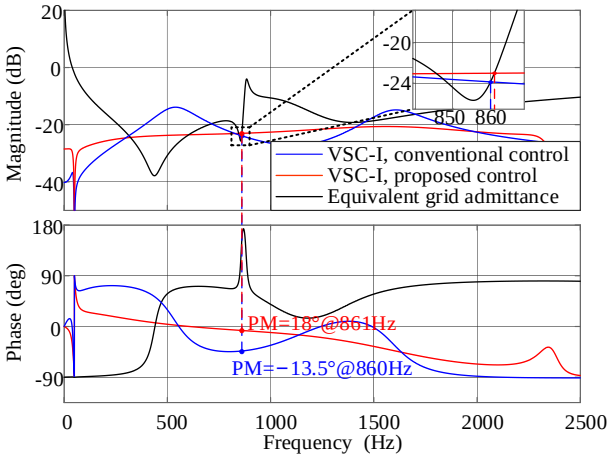

Fig. 14. Frequency responses of the equivalent grid admittance, and the VSC's output admittances using conventional control and the proposed control.

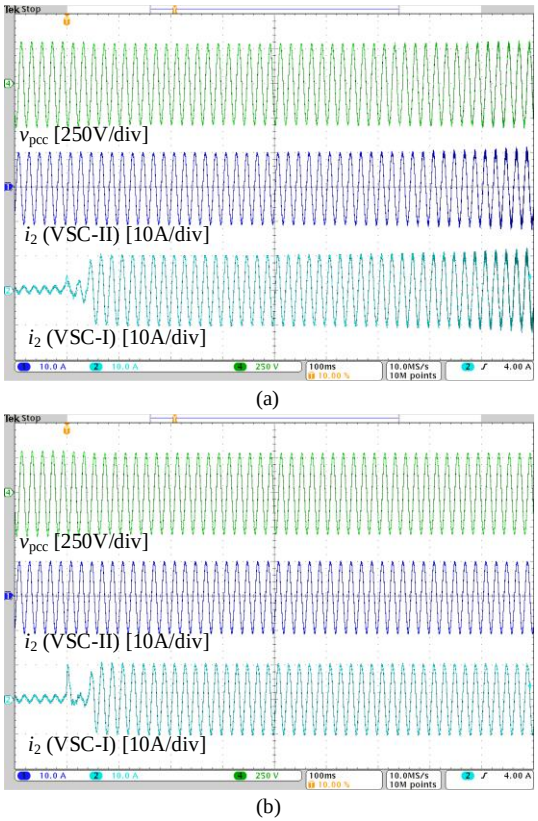

Fig. 15. Experimental results for stability verification using (a) conventional control, and (b) proposed state feedback control ($L_g = 4\ mH$, $C_g = 20\ \mu F$, and VSC-II connected).

$$Y_{g,eq}(s) = Y_{o1,VSC-II}(s) + Y_g(s) \quad (45)$$

Fig. 14 presents the Bode plots of $Y_{g,eq}(s)$, along with the output admittance of the VSC-I using conventional control and the proposed control. Obviously, the equivalent grid admittance is non-dissipative around the 17th order harmonic because of the non-dissipative VSC-II. The PMs in the distance of the 17th order harmonic are not marked out since they are all stable. Only the PMs around 17th order harmonic are marked out. As it can be seen, the PM of conventional control is negative indicating instability, whereas the PM of proposed control is positive indicating stability. The reason lies in the difference of their phase curves. The phase curve of proposed method is flatter and closer to zero compared with that of conventional control, and thus can provide more phase margin.

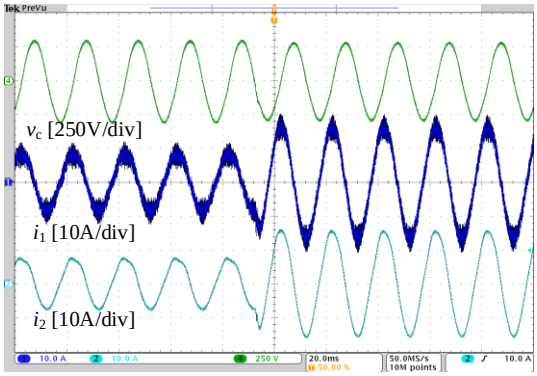

Fig. 16. Reference current step change performance using proposed state feedback control. ($L_g = 4\ mH$, $C_g = 20\ \mu F$)

The fact is further verified by experiments. Fig. 15(a) and (b) show the experimental results of the system using conventional control and proposed control respectively. In experiments, VSC-II is started first. After VSC-II enters steady state, VSC-I is enabled. As it can be seen, even though the divergence is slow, the waveform using conventional control (see Fig. 15(a)) become divergent at the end of the waveforms, whereas the waveform using proposed control (see Fig. 15(b)) remain stable. These two experiments verify the superior capabilities of the proposed control to the conventional control in stabilizing the non-dissipative grid impedance.

Additionally, it is notable that the initial current of the proposed state feedback method is significantly higher, at approximately 10A, than that of the conventional method, as shown in Fig. 11, Fig. 13, and Fig. 15. This is because, the CVF coefficient for the state feedback control is 1.8, leading to a substantial discrepancy between the output voltage and the capacitor voltage at the starting moment. This discrepancy results in a higher starting current compared to the conventional control, whose CVF coefficient is 0.9. Typically, addressing this issue of high starting current requires special starting technique like setting a specific initial value for the R controller. However, to keep the result faithful to the original setups, no modification has been made.

D. Current Reference Step Response

The experimental result of the current reference step response using the proposed state feedback control is shown in Fig. 16. Grid impedance adopting the combination of L_g and C_g as listed in Table I. VSC-II is disconnected from the grid, whereas VSC-I is connected to the grid using the proposed state-feedback control. Current reference steps from half load (7.5A) to full load (15A) increasing by 7.5A or 0.5 p.u.. As it can be seen, the system can operate stably with almost no current overshoot, and the transient time is about 2 ms. The proposed state feedback control can work well under both steady state and transient state. Besides, before the step change occur, the waveform of i_2 contains obvious harmonics. These harmonics are mostly 2nd and 4th order harmonics caused by sampling-induced switching harmonic aliasing. This issue can be tackled by multiple sampling or increasing switching frequency [37], [38].

V. Conclusion

This paper introduces an advanced state feedback control approach utilizing optimization methods to address the limitations of conventional non-optimal parameter tuning in passivity-based controller designs. The proposed state feedback control does not entail more sensors than the conventional control strategy. In line with the impedance-based stability criterion, an output admittance having a phase curve nearing zero and a reduced magnitude curve is beneficial to external stability. Thus, the optimization objective is formulated as the product of the 2-norms of the phase and magnitude curves of the output admittance, with the restriction of the VSC's internal stability. Due to the complexities of solving the feasible region in the *s*-domain, it is resolved in the *z*-domain instead. The resultant optimal state feedback control enhances system stabilization in the presence of non-dissipative grid impedance, and generally achieves dissipativity below the Nyquist frequency. The efficacy of this state feedback control method is demonstrated through experimental validation across various operating scenarios.

Appendix

r assumes its maximum, 1, and thus the (33) can be expressed as

$$\left|\frac{-b_1 \pm \sqrt{b_1^2 - 4c_1}}{2}\right| \leq 1 \tag{46}$$

The sign of $b_1^2 - 4c_1$ decides whether the two roots are real or not.

Situation 1: $b_1^2 - 4c_1 \geq 0$

In this situation, (46) infers that the quadratic equation: $f(\lambda) = \lambda^2 + b_1\lambda + c_1 = 0$ has two real roots within $[-1, 1]$. Therefore, $f(\lambda)$ crosses the λ-axis twice within $[-1, 1]$, and the following simultaneous inequality should hold

$$f(1) = 1 + b_1 + c_1 \geq 0 \tag{47}$$

$$f(-1) = 1 - b_1 + c_1 \geq 0 \tag{48}$$

$$-1 \leq -\frac{b_1}{2} \leq 1 \tag{49}$$

where (49) restricts the minimum point of $f(\lambda)$, i.e., $-\frac{b_1}{2}$, within $[-1, 1]$.

The solution is:

$$\mathrm{I} = \left(\begin{bmatrix} -1 & -1 \\ 1 & -1 \\ -1 & 0 \\ 1 & 0 \end{bmatrix}\begin{bmatrix} b_1 \\ c_1 \end{bmatrix} \leq \begin{bmatrix} 1 \\ 1 \\ 2 \\ 2 \end{bmatrix}\right) \bigcup (b_1^2 - 4c_1 > 0) \tag{50}$$

which can be visualized by the blue region (region I) in Fig. 6.

Situation 2: $b_1^2 - 4c_1 < 0$

In this situation, (46) infers that the quadratic equation: $f(\lambda) = \lambda^2 + b_1\lambda + c_1 = 0$ has two complex roots with a modulus smaller than or equal to one. The roots can be written in the form of real and imaginary parts:

$$\lambda_{1,2} = -\frac{b_1}{2} \pm i\frac{\sqrt{-(b_1^2 - 4c_1)}}{2} \tag{51}$$

The restriction on modulus requires:

$$\left(-\frac{b_1}{2}\right)^2 + \left(\frac{\sqrt{-(b_1^2 - 4c_1)}}{2}\right)^2 \leq 1 \tag{52}$$

Therefore, the solution of this situation is

$$\mathrm{II} = (c_1 \leq 1) \bigcup (b_1^2 - 4c_1 < 0) \tag{53}$$

which can be visualized by the red region (region II) in Fig. 6. The final solution is the union of the two situations, i.e.,

$$\mathrm{I} \bigcap \mathrm{II} = \left(\begin{bmatrix} -1 & -1 \\ 1 & -1 \\ 0 & 1 \end{bmatrix}\begin{bmatrix} b_1 \\ c_1 \end{bmatrix} \leq \begin{bmatrix} 1 \\ 1 \\ 1 \end{bmatrix}\right) \tag{54}$$

which is the triangular region in Fig. 6.

References

[1] Y. Liao, X. Wang, and F. Blaabjerg, "Passivity-based analysis and design of linear voltage controllers for voltage-source converters," *IEEE Open Journal of the Industrial Electronics Society*, vol. 1, no. 1, pp. 114–126, Jun. 2020.

[2] L. Harnefors, X. Wang, A. G. Yepes, and F. Blaabjerg, "Passivity-Based Stability Assessment of Grid-Connected VSCs-An Overview," *IEEE J Emerg Sel Top Power Electron*, vol. 4, no. 1, pp. 116–125, Mar. 2016.

[3] J. Sun, "Impedance-based stability criterion for grid-connected inverters," *IEEE Trans Power Electron*, vol. 26, no. 11, pp. 3075–3078, Nov. 2011.

[4] X. Wang, F. Blaabjerg, and W. Wu, "Modeling and analysis of harmonic stability in an AC power-electronics- based power system," *IEEE Trans Power Electron*, vol. 29, no. 12, pp. 6421–6432, Dec. 2014.

[5] L. Harnefors, L. Zhang, and M. Bongiorno, "Frequency-domain passivity-based current controller design," *IET Power Electronics*, vol. 1, no. 4, pp. 455–465, Dec. 2008.

[6] M. A. Awal, W. Yu, and I. Husain, "Passivity-based predictive-resonant current control for resonance damping in LCL-Equipped VSCs," *IEEE Trans Ind Appl*, vol. 56, no. 2, pp. 1702–1713, Mar. 2020.

[7] L. Harnefors, R. Finger, X. Wang, H. Bai, and F. Blaabjerg, "VSC Input-Admittance Modeling and Analysis above the Nyquist Frequency for Passivity-Based Stability Assessment," *IEEE Transactions on Industrial Electronics*, vol. 64, no. 8, pp. 6362–6370, Aug. 2017.

[8] L. Harnefors, A. G. Yepes, A. Vidal, and J. Doval-Gandoy, "Passivity-based stabilization of resonant current controllers with consideration of time delay," *IEEE Trans Power Electron*, vol. 29, no. 12, pp. 6260–6263, Dec. 2014.

[9] C. Gao, S. He, P. Davari, K. N. Leung, P. C. Loh, and F. Blaabjerg, "Passivity-Based Design of Resonant Current Controllers Without Involving Partial Derivative," *IEEE Trans Power Electron*, vol. 38, no. 12, pp. 15102–1518, Sep. 2023.

[10] X. Wang, F. Blaabjerg, and P. C. Loh, "Passivity-Based Stability Analysis and Damping Injection for Multiparalleled VSCs with LCL Filters," *IEEE Trans Power Electron*, vol. 32, no. 11, pp. 8922–8935, Nov. 2017.

[11] L. Harnefors, A. G. Yepes, A. Vidal, and J. Doval-Gandoy, "Passivity-based controller design of grid-connected VSCs for prevention of electrical resonance instability," *IEEE Transactions on Industrial Electronics*, vol. 62, no. 2, pp. 702–710, Feb. 2015.

[12] S. Li and H. Lin, "Passivity Enhancement-Based General Design of Capacitor Current Active Damping for LCL-Type Grid-Tied Inverter," *IEEE Trans Power Electron*, vol. 38, no. 7, pp. 8223–8236, Jul. 2023.

[13] X. Wang, Y. He, D. Pan, H. Zhang, Y. Ma, and X. Ruan, "Passivity Enhancement for LCL-Filtered Inverter With Grid Current Control and Capacitor Current Active Damping," *IEEE Trans Power Electron*, vol. 37, no. 4, pp. 3801–3812, Apr. 2022.

[14] C. Wang, X. Wang, Y. He, D. Pan, H. Zhang, X. Ruan, and X. Chen, "Passivity-Oriented Impedance Shaping for LCL-Filtered Grid-Connected Inverters," *IEEE Transactions on Industrial Electronics*, vol. 70, no. 9, pp. 9078–9090, Sep. 2023.

[15] X. Wang, K. Qin, X. Ruan, D. Pan, Y. He, and F. Liu, "A Robust Grid-Voltage Feedforward Scheme to Improve Adaptability of Grid-Connected Inverter to Weak Grid Condition," *IEEE Trans Power Electron*, vol. 36, no. 2, pp. 2384–2395, Feb. 2021.
[16] C. Wang, X. Wang, Y. He, and X. Ruan, "A Passivity-Based Weighted Proportional-Derivative Feedforward Scheme for Grid-Connected Inverters with Enhanced Harmonic Rejection Ability," *IEEE J Emerg Sel Top Power Electron*, vol. 11, no. 4, pp. 3656–3668, Aug. 2023.
[17] H. Wu and X. Wang, "Virtual-Flux-Based Passivation of Current Control for Grid-Connected VSCs," *IEEE Trans Power Electron*, vol. 35, no. 12, pp. 12673–12677, Dec. 2020.
[18] S. He, Z. Yang, D. Zhou, X. Wang, R. W. De Doncker, and F. Blaabjerg, "Dissipativity Robustness Enhancement for LCL-Filtered Grid-Connected VSCs With Multisampled Grid-Side Current Control," *IEEE Trans Power Electron*, vol. 38, no. 3, pp. 3992–4004, Mar. 2023.
[19] C. Xie, K. Li, J. Zou, D. Liu, and J. M. Guerrero, "Passivity-Based Design of Grid-Side Current-Controlled LCL-Type Grid-Connected Inverters," *IEEE Trans Power Electron*, vol. 35, no. 9, pp. 9815–9825, Sep. 2020.
[20] C. Xie, K. Li, J. Zou, and J. M. Guerrero, "Passivity-Based Stabilization of LCL-Type Grid-Connected Inverters via a General Admittance Model," *IEEE Trans Power Electron*, vol. 35, no. 6, pp. 6636–6648, Jun. 2020.
[21] S. He, D. Zhou, X. Wang, and F. Blaabjerg, "Passivity-Based Multisampled Converter-Side Current Control of LCL-Filtered VSCs," *IEEE Trans Power Electron*, vol. 37, no. 11, pp. 13848–13860, Nov. 2022.
[22] S. Cobreces, X. Wang, J. Perez, R. Grino, and F. Blaabjerg, "Robust Admittance Shaping Approach to Grid Current Harmonic Attenuation and Resonance Damping," *IEEE Trans Ind Appl*, vol. 54, no. 5, pp. 5039–5053, Sep. 2018.
[23] J. Perez, S. Cobreces, R. Grino, and F. J. R. Sanchez, "H∞ current controller for input admittance shaping of VSC-based grid applications," *IEEE Trans Power Electron*, vol. 32, no. 4, pp. 3180–3191, Apr. 2017.
[24] J. Serrano-Delgado, S. Cobreces, M. Rizo, and E. Bueno, "Low-Order Passivity-Based Robust Current Control Design for Grid-Tied VSCs," *IEEE Trans Power Electron*, vol. 36, no. 10, pp. 11886–11899, Oct. 2021.
[25] J. Serrano-Delgado, S. Cobreces, E. J. Bueno, and M. Rizo, "Passivity-based fixed-order h-infinity controller design for grid-forming VSCs," in *IEEE Applied Power Electronics Conference and Exposition*, 2021, pp. 2459–2466.
[26] Hui Yu, M A Awal, Hao Tu, Yuhua Du, Srdjan Lukic, and Iqbal Husain, "Passivity-Oriented Discrete-Time Voltage Controller Design for Grid-Forming Inverters," in *IEEE Energy Conversion Congress and Exposition (ECCE)*, 2019, pp. 469–475.
[27] P. Krus and J. Ölvander, "Performance index and meta-optimization of a direct search optimization method," *Engineering Optimization*, vol. 45, no. 10, pp. 1167–1185, Oct. 2013.
[28] L. Zhou and S. Bai, "A new approach to design of a lightweight anthropomorphic arm for service applications," *J Mech Robot*, vol. 7, no. 3, Aug. 2015.
[29] D. Pan, X. Ruan, C. Bao, W. Li, and X. Wang, "Capacitor-current-feedback active damping with reduced computation delay for improving robustness of LCL-type grid-connected inverter," *IEEE Trans Power Electron*, vol. 29, no. 7, pp. 3414–3427, Jul. 2014.
[30] S. He and F. Blaabjerg, "Design-Oriented Dissipativity Robustness Enhancement for Current Control of LCL- Filtered Grid-Following VSCs," in *Proc. IEEE Appl. Power Electron. Conf. Expo.*, 2023, pp. 2796–2800.
[31] H. J. Ko and J. J. P. Tsai, "Robust and Computationally Efficient Digital IIR Filter Synthesis and Stability Analysis under Finite Precision Implementations," *IEEE Transactions on Signal Processing*, vol. 68, pp. 1807–1822, Mar. 2020.
[32] D. Perez-Estevez, J. Doval-Gandoy, and J. M. Guerrero, "AC-Voltage Harmonic Control for Stand-Alone and Weak-Grid-Tied Converter," *IEEE Trans Ind Appl*, vol. 56, no. 1, pp. 403–421, Jan. 2020.
[33] T. H. S. Abdelaziz and M. Valášek, "Pole-placement for SISO linear systems by state-derivative feedback," *IEE Proceedings: Control Theory and Applications*, vol. 151, no. 4, pp. 377–385, Jul. 2004.
[34] D. Perez-Estevez, J. Doval-Gandoy, A. G. Yepes, O. Lopez, and F. Baneira, "Generalized multifrequency current controller for grid-connected converters with LCL filter," *IEEE Trans Ind Appl*, vol. 54, no. 5, pp. 4537–4553, Sep. 2018.
[35] H. Chung, H. Wang, F. Blaabjerg, and M. Pecht, *Reliability of power electronic converter systems*. Stevenage, UK: Institution of Engineering and Technology, 2015.
[36] C. R. D. Osório, G. G. Koch, H. Pinheiro, R. C. L. F. Oliveira, and V. F. Montagner, "Robust Current Control of Grid-Tied Inverters Affected by LCL Filter Soft-Saturation," *IEEE Transactions on Industrial Electronics*, vol. 67, no. 8, pp. 6550–6561, Aug. 2020.
[37] R. Li, B. Liu, S. Duan, C. Zou, and L. Jiang, "Analysis and suppression of alias in digitally controlled inverters," *IEEE Trans Industr Inform*, vol. 10, no. 1, pp. 655–665, Feb. 2014.
[38] B. Zhang, J. Xu, and S. Xie, "Analysis and suppression of the aliasing in real-time sampling for grid-connected LCL-filtered inverters," in *Proceedings of the 2016 IEEE 11th Conference on Industrial Electronics and Applications (ICIEA)*, Hefei, China, 2016, pp. 304–309.

Chao Gao received the B.S. degree from Wuhan University, Wuhan, China, in 2018, and the M.S. degree from Huazhong University of Science and Technology, Wuhan, China, in 2021, both in electrical engineering. He is currently working toward the Ph.D. degree from the Chinese University of Hong Kong, Hong Kong. He is guest Ph.D. Student with the Department of Energy, Aalborg University, Aalborg, Denmark since 2023. His research interests include modeling and control of power electronic converters.

Shan He (Member, IEEE) received the B.S. degree from Northeast Electric Power University, Jilin, China, in 2015, the M.S. degree from Zhejiang University, Hangzhou, China, in 2018, and the Ph.D. from Aalborg University, Aalborg, Denmark, in 2022, all in electrical engineering. His research interests include power electronics-based power system stability, grid-connected renewable system, Power to X, and battery management system.

In 2021, he was a visiting researcher with Institute for Power Generation and Storage Systems, RWTH Aachen University, Aachen, Germany. From 2023-2024, he was a research associate with Chair of Power Electronics, Kiel University, Kiel, Germany. He was the recipient of IES-SYPA in 2023. He is the Associate Editor of Protection and Control of Modern Power Systems and session chair for several IEEE conferences.

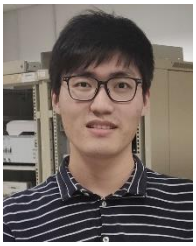

Peiji Song received the B.S. degree in optoelectronic information engineering from the Huazhong University of Science and Technology, Wuhan, China, in 2019, and the Ph.D. degree in information engineering from The Chinese University of Hong Kong, Hong Kong, in 2024. From Jul 2023 to Oct 2023, he worked as a Summer Intern in Nokia Bell Labs. His research interests include passive optical networks, advanced modulation formats, and digital signal processing for optical systems.

Pooya Davari (S'11–M'13-SM'19) received the B.Sc. and M.Sc. degrees in electronic engineering in 2004 and 2008, respectively from University of Mazandaran, Iran, and the Ph.D. degree in power electronics from QUT, Australia, in 2013. From 2005 to 2010, he was involved in several electronics and power electronics projects as a Development Engineer. From 2013 to 2014, he was with QUT, as a Lecturer. He joined Aalborg University (AAU), in 2014, as a Postdoc, where he is currently an Associate Professor.

He has been focusing on EMI, power quality and harmonic mitigation analysis and control in power electronic systems. He has published more than 200 technical papers. He is an Associate Editor of IEEE Transactions on Transportation Electrification, IEEE Transactions on Power Electronics, Journal of Emerging and Selected Topics in Power Electronics, journal of Power Electronics, IET Electronics, Editorial board member of Journal of Applied Sciences and Journal of Magnetics. He is a member of Joint Working Group six and Working Group eight at the IEC standardization TC77A. Dr. Davari is the recipient of Equinor 2022 Prize (Denmark oldest engineering award) and 2020 IEEE EMC Society Young Professional Award for his contribution to EMI and Harmonic Mitigation and Modeling in Power Electronic Applications. He is currently Editor-in-Chief of Circuit World Journal. He is founder and chair of IEEE EMC SOCIETY CHAPTER DENMARK, Leader of EMI/EMC in Power Electronics Research Group, and vice chair of Energy Efficiency Mission at AAU Energy.

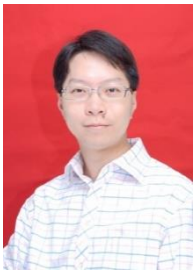

Ka Nang Leung (Senior Member, IEEE) received the B.Eng., M.Phil., and Ph.D. degrees in Electrical and Electronic Engineering from Hong Kong University of Science and Technology (HKUST), Clear Water Bay, Hong Kong, in 1996, 1998, and 2002, respectively. In 2002, he was a Visiting Assistant Professor at HKUST. In 2005, he joined with the Department of Electronic Engineering, Chinese University of Hong Kong, Hong Kong, where he is currently an Associate Professor. His research interests include power-management integrated circuits and low-voltage low-power analog integrated circuits.

Dr. Leung is the Chairperson of the IEEE (Hong Kong) Electron Device/Solid-State Circuit Joint Chapter in 2012. He is a senior member of IEEE. He is a member in the Editorial Board and a guest editor of a special issue of Energies. He serves as a Paper Reviewer in numerous IEEE journals and IEEE international conferences. Moreover, he is actively involved in the organization of IEEE international conferences. He is a co-recipient of the Silkroad Award of ISSCC in 2024, the Best Paper Awards of TENCON in 2015 and the IEEE Student Symposium ED/SSC in 2011, 2014 and 2019.

Poh Chiang Loh received the B.Eng. (hons.) and M.Eng. degrees from the National University of Singapore, Singapore, in 1998 and 2000, respectively, and the Ph.D. degree from Monash University, Melbourne, Vic, Australia, in 2002, all in electrical engineering.

From 2013 to 2015, he was a Professor with Aalborg University, Aalborg, Denmark. Since 2015, he has been a Tenured Full Professor with the Chinese University of Hong Kong, Hong Kong, China. His research interests include power converters and their grid applications.

Frede Blaabjerg (S'86–M'88–SM'97–F'03) was with ABB-Scandia, Randers, Denmark, from 1987 to 1988. From 1988 to 1992, he got the PhD degree in Electrical Engineering at Aalborg University in 1995. He became an Assistant Professor in 1992, an Associate Professor in 1996, and a Full Professor of power electronics and drives in 1998 at AAU Energy. From 2017 he became a Villum Investigator. He is honoris causa at University Politehnica Timisoara (UPT), Romania in 2017 and Tallinn Technical University (TTU), Estonia in 2018.

His current research interests include power electronics and its applications such as in wind turbines, PV systems, reliability, Power-2-X, power quality and adjustable speed drives. He has published more than 600 journal papers in the fields of power electronics and its applications. He is the co-author of eight monographs and editor of fourteen books in power electronics and its applications eg. the series (4 volumes) Control of Power Electronic Converters and Systems published by Academic Press/Elsevier.

He has received 38 IEEE Prize Paper Awards, the IEEE PELS Distinguished Service Award in 2009, the EPE-PEMC Council Award in 2010, the IEEE William E. Newell Power Electronics Award 2014, the Villum Kann Rasmussen Research Award 2014, the Global Energy Prize in 2019 and the 2020 IEEE Edison Medal. He was the Editor-in-Chief of the IEEE TRANSACTIONS ON POWER ELECTRONICS from 2006 to 2012. He has been Distinguished Lecturer for the IEEE Power Electronics Society from 2005 to 2007 and for the IEEE Industry Applications Society from 2010 to 2011 as well as 2017 to 2018. In 2019-2020 he served as a President of IEEE Power Electronics Society. He has been Vice-President of the Danish Academy of Technical Sciences. He is nominated in 2014-2021 by Thomson Reuters to be between the most 250 cited researchers in Engineering in the world.